Preparation of Ce–Mn Composite Oxides with Enhanced Catalytic Activity for Removal of Benzene through Oxalate Method

Min Yang [1,†], Genli Shen [2,†], Mi Liu [2], Yunfa Chen [3], Zhen Wang [2,*] and Qi Wang [2,*]

[1]   Department of Chemistry, School of Chemistry and Biological Engineering,
      University of Science and Technology, Beijing 100083, China; yangmin@ustb.edu.cn
[2]   CAS Key Laboratory of Standardization and Measurement for Nanotechnology,
      CAS Center for Excellence in Nanaoscience, National Center for Nanoscience and Technology,
      Beijing 100190, China; shengl@nanoctr.cn (G.S.); liumi@nanoctr.cn (M.L.)
[3]   State Key Laboratory of Multiphase Complex Systems, Institute of Process Engineering,
      Chinese Academy of Sciences, Beijing 100190, China; yfchen@home.ipe.ac.cn
*   Correspondence: wangzh@nanoctr.cn (Z.W.); wangq@nanoctr.cn (Q.W.);
      Tel.: +86-10-82545755 (Z.W.); Fax: +86-10-62525716 (Z.W. & Q.W.)
†   Those authors contributed equally to this work.

check for updates

Abstract: The catalytic activities of CeO_2-MnO_x composite oxides synthesized through oxalate method were researched. The results exhibited that the catalytic properties of CeO_2-MnO_x composite oxides were higher than pure CeO_2 or MnO_x. When the Ce_{at}/Mn_{at} ratio was 3:7, the catalytic activity reached the best. In addition, the activities of CeO_2-MnO_x synthesized through different routes over benzene oxidation were also comparative researched. The result indicated that the catalytic property of sample prepared by oxalate method was better than others, which maybe closely related with their meso-structures. Meanwhile, the effects of synergistic interaction and oxygen species in the samples on the catalytic ability can't be ignored.

Keywords: CeO_2-MnO_x composite oxides; oxalate method; mesoporous structure; benzene oxidation

1. Introduction

Volatile organic compounds (VOCs) produced by industrial manufacturing are an important class of air pollutants. Among the VOCs, aromatic compounds are one of the major hazardous pollutants, in which benzene is considered to be one of the representing aromatic materials extensively applied in the industry. The complete catalytic oxidation of benzene is often studied as a model reaction, characteristic of the catalytic combustion of VOCs due to its chemical stability [1–5]. The selection of catalysts is important to catalytic degradation of benzene. At present, both classes of catalysts i.e., noble metals and transition metal oxides, have been widely studied for the degradation of VOCs [6–9]. However, the usage of noble-metal-based catalysts is limited due to high cost, low thermal stability and sensitivity to poisoning. Transition metal oxide-based catalysts are suitable alternative because of higher thermal stability and lower price [10]. In certain cases, transition metal oxides can be actually more active than noble metal catalysts [11].

Ceria (CeO_2), as a typical rare earth oxide, was investigated in heterogeneous catalysis field due to its high oxygen storage capacity. It can provide active oxygen species to ensure the catalytic reaction. More recently, CeO_2-based composite oxides were employed for VOCs removal and obtain satisfied results, especially Ce-Mn composites [12–14]. CeO_2-MnO_x can be applied as heterogeneous catalysts for the abatement of contaminants in the liquid and gas phases, such as the catalytic reduction of NO

and oxidation of acrylic acid and formaldehyde, which exhibit much higher catalytic activity than those of pure MnO_x and CeO_2 [15–18].

In our previous work [19], Mn element was also doped or mixed with CeO_2 to obtain Ce-Mn composites through hydrothermal method. Their catalytic behaviours over benzene oxidation were researched, among which, all of Ce-Mn composites exhibited higher activity than MnO_x and CeO_2. However, the best conversion temperature of benzene oxidation over Ce-Mn composite was ca. 375 °C, which could not be applied in the moderate or lower temperature range (100–200 °C) [19], even if supporting noble metal species [20]. Therefore, we need to prepare catalysts with better performance through adjusting microstructure. In this article, we report a series of Ce-Mn composites synthesized through different routes. Their catalytic activities over benzene oxidation are researched comparatively so as to acquire more active catalyst in the temperature range of 100 and 200 °C. Their microstructures are also analyzed in detail so that understanding the elements influencing the activity of samples.

2. Experimental

2.1. The Preparation of Ce-Mn Composite Oxides

The chemicals used in this work, including $Ce(NO_3)_3 \cdot 6H_2O$ (99%), $Mn(CH_3COO)_2 \cdot 4H_2O$, Na_2CO_3, $C_2H_2O_4 \cdot 2H_2O$, NaOH (98%), and ethanol, were purchased from Beijing Chemicals Company (Beijing, China). A series of Ce-Mn composite oxides were synthesized by carbonate method. Briefly, $Ce(NO_3)_3 \cdot 6H_2O$ and $Mn(CH_3COO)_2 \cdot 4H_2O$ in appreciate amounts were dissolved in a 100 mL H_2O and mixed with a 0.24 M $C_2H_2O_4 \cdot 2H_2O$ solution under strong stirring. Then, the mixture was stirred for another 1 h. The precipitates were collected by centrifugation, washed with distilled water and ethanol several times. The obtained materials, labeled as Ce_xMn_{1-x} (where x refers to the $Ce/(Ce + Mn)$ atomic ratio) were dried at 80 °C overnight and calcined at 450 °C for 2 h with a heating rate of 2 °C·min^{-1}. Pure CeO_2 and MnO_x were also prepared using the similar process as reference. In order to compare the catalytic activity, Ce-Mn composite oxides were also synthesized through carbonate method and hydrothermal method [19,21].

2.2. Characterization Technique

The crystal phase of the materials was characterized on X-ray diffraction (XRD, Philips, Amsterdam, The Netherlands) equipped with a Cu $K\alpha$ radiation source (λ = 0.154187 nm) at a scanning rate of 0.03 °/s (2θ from 10° to 90°). The assignment of the crystalline phases was based on the ICSD data base (CeO_2 no. 81-0792; Mn_3O_4 no. 80-0382; Mn_2O_3 no. 89-4836). The morphology images of catalysts were recorded on a scanning electron microscopy (SEM, JEOL JSM-6700F, Tokyo, Japan) operating at 15 kV and 10 μA. The microstructures of catalysts were examined using transmission electron microscopy (TEM, JEOL JEM-2010F) with an accelerating voltage of 200 kV.

The BET specific surface area (S_{BET}) was measured by physical adsorption of N_2 at the liquid nitrogen temperature using an Autosorb-1 analyzer (Quantachrome, Boynton Beach, FL, USA). Before measurement, the samples were degassed at 300 °C for 4 h under vacuum. Surface composition was determined by X-ray photoelectron spectroscopy (XPS, VG Scientific, Waltham, MA, USA) using an ESCALab220i-XL electron spectrometer from VG Scientific with a monochromatic Al $K\alpha$ radiation. The binding energy (BE) was referenced to the C1s line at 284.8 eV from adventitious carbon.

Hydrogen temperature-programmed reduction (H_2-TPR) was performed with a U-type quartz reactor equipped with Automated Catalyst Characterization System (Autochem 2920, MICROMERITICS). A 50 mg sample (40–60 mesh) was loaded and pretreated with a 5% O_2 and 95% He mixture (30 mL/min) at 150 °C for 1 h and cooled to 50 °C under He flow. The samples were then heated to 900 °C at a rate of 10 °C/min under the flow of a 10% H_2 and 90% Ar mixture (30 mL/min).

2.3. Catalytic Activity Tests

Activity tests for catalytic oxidation of benzene over Ce_xMn_{1-x} composite catalysts were performed in a continuous-flow fixed-bed reactor under atmospheric pressure, containing 100 mg of catalyst samples (40–60 mesh). A standard reaction gas containing 1000 ppm benzene and 20% O_2 in N_2 was fed with a total flow rate of 100 mL/min. The weight hourly space velocity (WHSV) was typically 60,000 mL·g^{-1}·h^{-1}. The reactants and the products were analyzed on-line using a GC/MS 6890N gas chromatograph (Hewlett-Packard, Palo Alto, CA, USA) interfaced to a 5973N mass selective detector (Hewlett-Packard, Palo Alto, USA) with a HP-5MS capillary column (30 m × 0.25 mm × 0.25 µm) and another GC (GC112A, Shangfen, Shanghai, China) with a carbon molecule sieve column. The conversion of benzene ($X_{benzene}$, %) was calculated as follows:

$$X_{benzene} = \frac{C_{benzene(in)} - C_{benzene(out)}}{C_{benzene(in)}} \times 100\% \tag{1}$$

where, $C_{benzene\,(in)}$ (ppm) and $C_{benzene\,(out)}$ (ppm) are the concentrations of benzene in the inlet and outlet gas, respectively.

3. Results and Discussion

3.1. Catalytic Oxidation Activity of Ce_xMn_{1-x} Composite Oxides for Benzene

The catalytic performance of CeO_2, MnO_x and Ce_xMn_{1-x} catalysts was evaluated through the oxidation of benzene. The catalytic conversion of benzene as a function of the temperature, 100–400 °C, is shown in Figure 1a. It can be acquired that MnO_x exhibits the least active followed by CeO_2. With the Mn element adding into CeO_2, the activity increases monotonically up to a Mn content of 70 at.% and $Ce_{0.3}Mn_{0.7}$ is the most active among all catalysts achieving complete benzene conversion at ca. 200 °C. The MnO_x and CeO_2 catalysts synthesized through oxalate route also achieve full conversion at ca. 300 °C. In addition, the activities of $Ce_{0.3}Mn_{0.7}$ synthesized through different routes over benzene oxidation are comparative researched in order to identify the advantage of oxalate route (Figure 1b). The result indicates that the sample exhibits higher activity than that of corresponding samples synthesized by hydrothermal or carbonate routes, which is probably related with the microstructure of catalyst. For the purposes of comparison, the reaction temperatures $T_{10\%}$, $T_{50\%}$, $T_{90\%}$ (corresponding to the benzene conversion = 10%, 50%, 90%) used to evaluate the performances of the catalysts are summarized in Table 1.
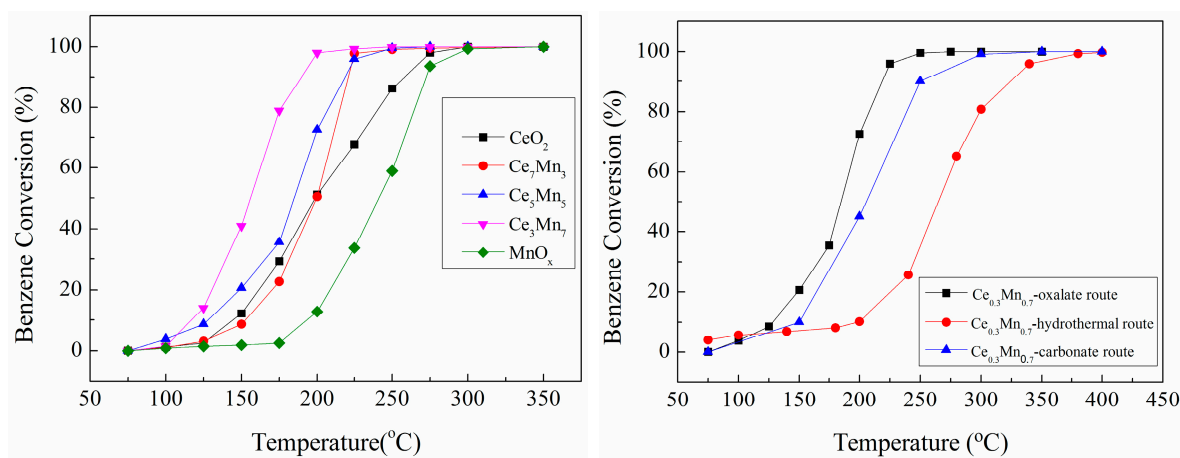

Figure 1. C_6H_6 conversion (%, (**a**)) over CeO_2, MnO_x and Ce_xMn_{1-x} catalysts synthesized by oxalate method; C_6H_6 conversion comparison as a function of reaction temperature over Ce_3Mn_7 through different reaction route (**b**).

Table 1. Catalytic activities of CeO_2, MnO_x and Ce_xMn_{1-x} catalysts.

Catalyst	Benzene Oxidation Activity		
	$T_{10\%}$ (°C)	$T_{50\%}$ (°C)	$T_{90\%}$ (°C)
CeO_2	145	200	257
$Ce_{0.7}Mn_{0.3}$	153	200	220
$Ce_{0.5}Mn_{0.5}$	128	185	218
$Ce_{0.3}Mn_{0.7}$	117	156	190
MnO_x	194	241	273
$Ce_{0.3}Mn_{0.7}$ (Hydrothermal)	200	265	350
$Ce_{0.3}Mn_{0.7}$ (Carbonate)	150	220	250

3.2. Characterization of Ce_xMn_{1-x} Catalysts

Figure 2a shows the XRD patterns of the samples in the angular range 10–70 2θ. The diffraction peaks at 2θ = 28.5, 33.0, 47.4, 56.4 and 59.2 in the XRD profile of the pure cerium oxide clearly demonstrate the presence of cubic fluorite structure of CeO_2 (JCPDS 81-0792). For pure MnO_x, the XRD pattern exhibits complex diffraction peaks which can be considered as a mixture of crystalline Mn_3O_4 (JCPDS 80-0382) and Mn_2O_3 (JCPDS 89-4836). The data demonstrates that manganese oxide is a multivalent framework manganese (2^+ and 3^+), which indicates the existence of various manganese oxides. For Ce_xMn_{1-x} catalyst, the XRD patterns exhibit more complex. The XRD patterns of the Ce_xMn_{1-x} mixed oxide (x ≥ 0.5) do not show any diffraction of manganese oxides, and only broad reflections attributed to CeO_2 are observed, which is possible to be related with the formation of solid solution between MnO_x and CeO_2. The diffraction patterns of Ce_xMn_{1-x} mixed oxides at x ≤ 0.3 show crystallization of Mn_3O_4 and Mn_2O_3 except that of CeO_2.

The formation of solid solution between MnO_x and CeO_2 can be further evidenced by the fact that the characteristic diffraction peak of CeO_2 in the composite oxides is slightly shifted to higher values of the Bragg angles, compared with the pure CeO_2 (Figure 2b). Since the ionic radius of Mn^{2+} (0.091 nm) and Mn^{3+} (0.066 nm) are both smaller than that of the Ce^{4+} (0.1098 nm), the incorporation of Mn^{2+} or Mn^{3+} into the CeO_2 lattice to form CeO_2-MnO_x solid solution would result in remarkable decrease in the lattice parameter of CeO_2 in the Ce_xMn_{1-x} composite oxide. Meanwhile the O vacancy is also easier to form in order to balance charge due to Ce^{4+} replaced by Mn^{2+} or Mn^{3+} in the Ce_xMn_{1-x} catalyst. The oxygen vacancy is beneficial to catalytic activities of Ce_xMn_{1-x} catalyst [19].
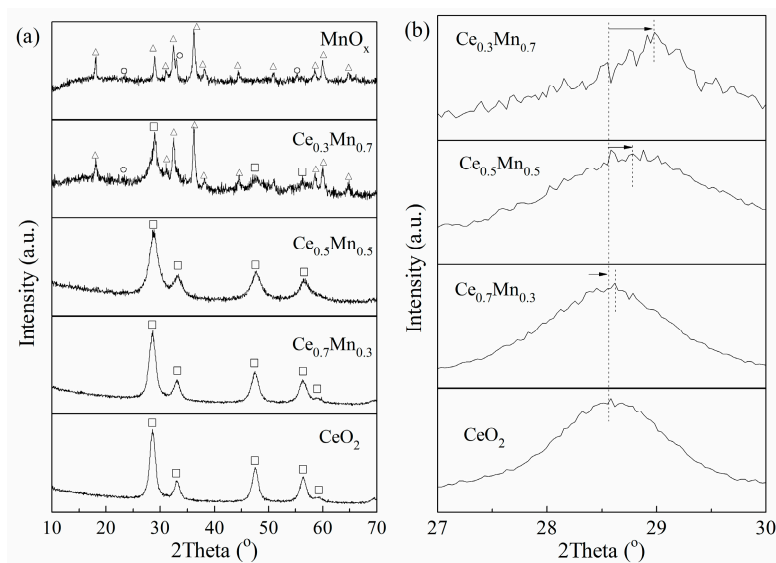

Figure 2. XRD patterns of all the samples: (**a**) wild angle patterns, and (**b**) Enlarged-zone patterns. Crystalline phases detected: (o) CeO_2, (□) Mn_3O_4, (Δ) Mn_2O_3.

The SEM images of as-prepared Ce_xMn_{1-x} oxide catalysts are presented in Figure 3a. For pure oxide CeO_2, it can be seen that the catalyst is composed of many thin flakes, which are overlapped together to form butterfly-like structure (inset picture). The thickness of every flake is about 200 nm and the length can extend to several micrometers. In the SEM image of MnO_x, a lot of grains with ellipsoid-like morphology are seen clearly and the size is ca.10 μm. At the surface of every grain, deep ravines are also obviously observed (inset picture). For Ce_xMn_{1-x} composite catalysts, the morphology changes gradually with the Mn content increasing. When the Mn theoretical content reaches 50% ($Ce_{0.5}Mn_{0.5}$), a few of bulk-like particles with size of several micrometers can be detected except thin flakes. When the theoretical content of Mn ion reaches to 70% ($Ce_{0.3}Mn_{0.7}$), a large number of grains possessing layered structure can be observed. In addition, it can be acquired that Ce, Mn and O elements are dispersed together homogeneously through element distribution over Ce_xMn_{1-x} composite catalysts.

Through the discussion over catalytic activities of Ce_xMn_{1-x}, it has been acquired that $Ce_{0.3}Mn_{0.7}$ presents the highest activity and preparation route is also important to the property of catalyst. Therefore, the TEM images of $Ce_{0.3}Mn_{0.7}$ prepared through different technology routes are shown so as to analyze their microstructures (Figure 3b). In the TEM image of $Ce_{0.3}Mn_{0.7}$ synthesized by oxalate route, the catalyst is composed of thin flakes. At the surface of flake, some mesoporous structures can be observed and the size of mesoporous is ca. 2 nm. As we known, the oxalate chains chelated in the corresponding precursors are easy to be decomposed into CO_x and H_2O with calcination in air, which can leave behind large numbers of voids due to the release of gaseous CO_x and H_2O [21]. Meanwhile, some primary nanoparticles are assembled together thereby forming porous structure, which is beneficial to absorb and desorb the gas due to the formation of massive active sites and decrease of mass transfer effect [22,23]. For $Ce_{0.3}Mn_{0.7}$ synthesized by carbonate route, some grains with dumbbell shape can be seen, which are composed of some stacked nanoparticles with the size of 1–2 nm. In the TEM of $Ce_{0.3}Mn_{0.7}$ prepared through hydrothermal method, a lot of nanorods with the diameter of ca. 10 nm and the length of 300–400 nm are observed, which is also composed of some assembled nanoparticles.

In addition, the N_2 adsorption–desorption isotherms and the pore size distribution of the as-prepared catalysts are displayed in Figure S1. The data show that the isotherms of the as-prepared materials possess type IV characteristics with well-developed H3 type hysteresis loops. The result indicates that the Ce_xMn_{1-x} composite catalysts possess porous structure, which is consistent with the result of SEM. The porous structure can facilitate the adsorption and diffusion of reactive molecules, thus greatly reducing limitations of inter-phase mass transfer and enhancing their catalytic activities [21].
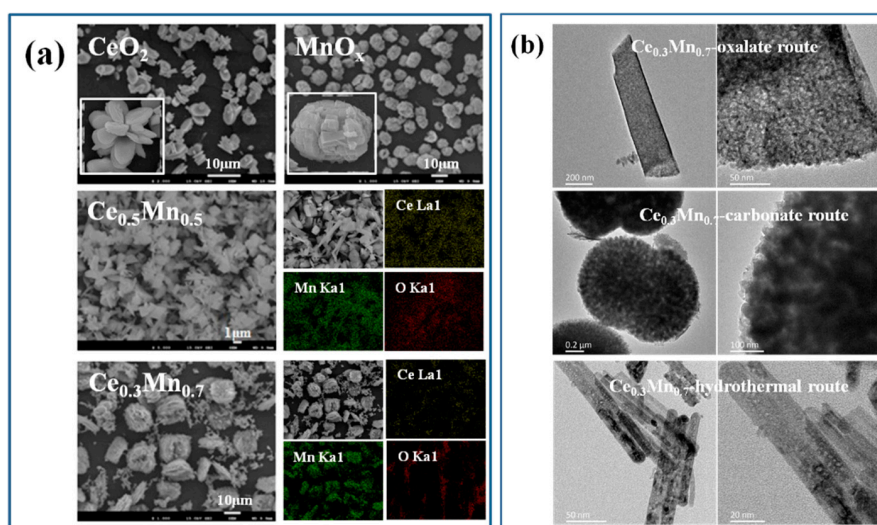

Figure 3. SEM images and EDX mapping of CeO_2, MnO_x, $Ce_{0.5}Mn_{0.5}$ and $Ce_{0.3}Mn_{0.7}$ (**a**); TEM images of $Ce_{0.3}Mn_{0.7}$ synthesized through different routes (**b**).

The oxidation state of catalyst surface species was examined by XPS analysis. Figure 4 exhibits XPS patterns of Ce 3d, Mn 2p, Mn 3s and O 1s for samples, respectively. In the Ce 3d spectrum of support (Figure 4a), six peaks labeled as V_0 (882.1 eV), V_1 (888.7 eV), V_2 (898.1 eV), V_0' (900.7 eV), V_1' (907.1 eV) and V_2' (916.3 eV) can be identified as characteristic of Ce^{4+} 3d final states [24,25]. The high BE doublet (V_2/V_2') is attributed to the final state of $Ce(IV)3d^94f^0O2p^6$, doublet V_1/V_1' is originated from the state of $Ce(IV)3d^94f^1O2p^5$, and doublet V_0/V_0' corresponds to the state of $Ce(IV)3d^94f^2O2p^4$. The character peaks of Ce^{3+} are also observed at 903.4/884.7 eV and 897.6/879.3 eV labeled as U_1/U_1' and U_0/U_0', respectively [26]. The amount of Ce^{3+} is estimated to be 11.05, 10.89, 10.05 and 5.65% for CeO_2, $Ce_{0.7}Mn_{0.3}$, $Ce_{0.5}Mn_{0.5}$ and $Ce_{0.3}Mn_{0.7}$, which can be calculated according to the Equation (2). Therefore, Ce species in the Ce_xMn_{1-x} composite oxides exist mainly in tetravalent oxidation state.

$$X_{Ce^{3+}} = \frac{A_{Ce^{3+}}/S_{Ce}}{\sum A_{(Ce^{3+}+Ce^{4+})}/S_{Ce}} \times 100\% \tag{2}$$

where $X_{Ce^{3+}}$ is the percentage content of Ce^{3+}, A is the integrate area of characteristic peak in the XPS pattern, S is sensitivity factors ($S = 7.399$).

Figure 4 shows the Mn 2p XPS spectra of Ce_xMn_{1-x} composite oxides, in which Mn 2p doublet can be distinguished. The binding energies of the Mn $2p_{3/2}$ component appear at 641.7 eV and those for Mn $2p_{1/2}$ appear at 653.2 eV. The BE values of the Mn $2p_{3/2}$ (641.7 eV) and spin–orbit splitting (11.7 eV) are well matching with the reported values of the trivalent manganese [27]. The shoulder of the Mn $2p_{3/2}$ component at 640.7 eV is attributed to Mn^{2+} species [28]. The XPS results do not provide any evidence for the presence of Mn^{4+} species (642.2–643 eV) [29,30]. In order to determine the chemical states of Mn further, Mn 3s XPS spectra of Ce_xMn_{1-x} are analyzed (Figure 4c). The spin−orbit splitting value (ΔEs) between the two doublets was 5.44 eV for all samples, closing to the value of 5.1 for the standard sample of α-Mn_2O_3. The ΔEs of MnO is about 6.3 eV, indicating that the oxidation status of Mn is predominantly tervalent [31,32]. The average oxidation state of Mn was calculated using formula $A_{OS} = 8.95 - 1.13 \times \Delta Es$ [33]. The data was calculated to be 2.80 that fall in between the average oxidation state of Mn (+2.67) in Mn_3O_4 and the state of Mn (+3) in Mn_2O_3. Therefore, the element Mn in the Ce_xMn_{1-x} catalysts is existed in the form of Mn_3O_4 and Mn_2O_3, which is consistent with the data of XRD. In addition, the peak of Mn 2p3/2 (641.5 eV) for Ce_xMn_{1-x} composites is shifted to lower binding energy comparing with pure MnO_x, which may be a consequence of interaction between CeO_2 and MnO_x [19]. It is worthy to note that the pattern and the intensity of $Ce_{0.7}Mn_{0.3}$ is similar and less weaker compared with other Ce_xMn_{1-x} composites. The corresponding XPS spectrum can be seen in the Figure S2.

The XPS O1s spectra (Figure 4d) show a main peak at a binding energy of 529.1–529.9 eV, corresponding to lattice oxygen of CeO_2 and MnO_x phases(O^{2-}; denoted as O_α) [27,30]. A broad shoulder at the higher binding energy region (531.3–531.8 eV) is ascribed to defective oxides or oxygen species of the surface carbonates and hydroxide (denoted as O_β) [18,34]. It is worthy to note that the peak corresponding to lattice oxygen in Ce_xMn_{1-x} composite catalyst with higher Mn content tends to shift toward higher BE value than that of pure CeO_2 (from 529.1 eV to 529.6 eV), which suggests that the environments of oxygen change with increasing Mn content. This appearance is also attributed to the interaction between CeO_2 and MnO_x. In addition, the content of O_α is calculated according to the Equation (3) and listed in Table 2. The data shows that the $Ce_{0.3}Mn_{0.7}$ sample possesses more lattice oxygen species, confirming that the mobility and availability of lattice oxygen species are enhanced due to the synergistic effects of CeO_2 and MnO_x in $Ce_{0.3}Mn_{0.7}$ [35].

$$X_{O_\alpha} = \frac{A_{O_\alpha}/S_O}{\sum A_{(O_\alpha+O_\beta)}/S_O} \times 100\% \tag{3}$$

where X_{O_α} is the percentage content of O_α, A is the integrate area of characteristic peak in the XPS pattern, S is sensitivity factors ($S = 0.711$).
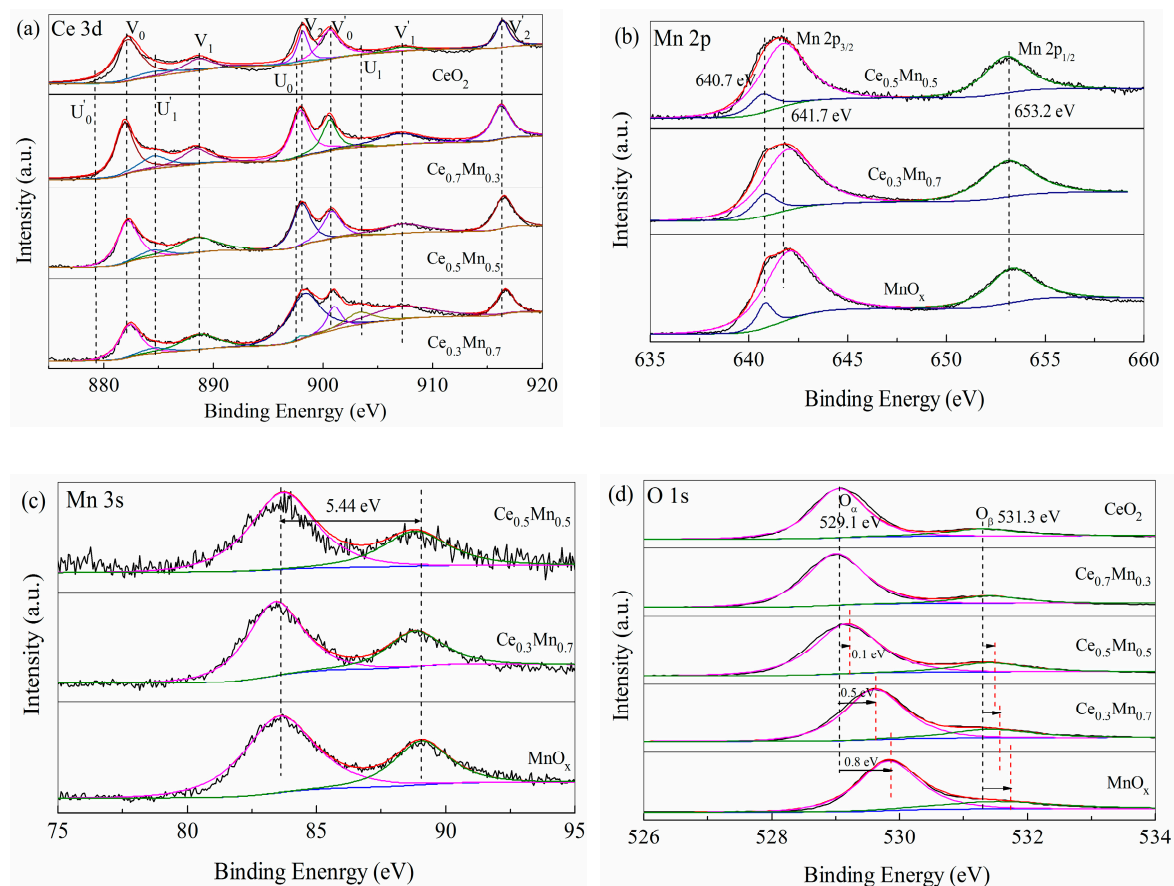
Figure 4. X-ray photoelectron spectra in the Ce 3d (**a**), Mn 2p (**b**), Mn 3s (**c**), O 1s (**d**) regions for the Ce_xMn_{1-x} catalysts.

Table 2. XPS results of Ce_xMn_{1-x} samples.

Sample	O		$O_\alpha/(O_\alpha + O_\beta)$ (%)	Ce (%)	Mn (%)
	O_α	O_β		$Ce^{3+}/(Ce^{3+} + Ce^{4+})$	$Mn^{2+}/(Mn^{2+} + Mn^{3+})$
CeO_2	529.0	531.3	77.16	11.05	-
$Ce_{0.7}Mn_{0.3}$	529.1	531.3	81.01	10.89	16.23
$Ce_{0.5}Mn_{0.5}$	529.1	531.3	82.04	10.05	15.12
$Ce_{0.3}Mn_{0.7}$	529.2	531.5	83.18	5.65	13.42
MnO_x	529.6	531.6	78.47	-	10.69

In order to check the redox properties of the new series of Ce_xMn_{1-x} systems, TPR of all the catalysts were carried out. Figure 5a shows the H_2-TPR profiles of CeO_2, MnO_x and Ce_xMn_{1-x} composite oxides. Similar to previous findings [36–38], pure CeO_2 exhibits two reduction peaks at around 405 °C and about 719 °C. The former low-temperature reduction is due to the removal of surface oxygen and the later high-temperature reduction is related to the oxygen species in bulk CeO_2. The H_2-TPR profile of pure MnO_x shows two strong reduction peaks at 167 °C and 330 °C, respectively, with an area ratio of the lower to the higher temperature hydrogen consumption of about 1:2.42. The actual hydrogen consumption of two reduction peaks is 0.92343 and 1.88118 mmol/g and the corresponding ratio is 1:2.04. As we known, Mn_2O_3 proceed two-step reduction, the low-temperature reduction peak represented the reduction of Mn_2O_3 to Mn_3O_4 and the high-temperature reduction peak referred to the further reduction of Mn_3O_4 to MnO [39]. The theoretical hydrogen consumption ratio is 1:2 as seen in Formula (4) and (5), which is less than the fitted value (2.42) and actual data (2.04). It indicates that the hydrogen gas is more consumed at higher temperature, which is attributed

to the extra existence of Mn_3O_4 phase. This is in agreement with the XRD data, which show that the crystalline phase of pure MnO_x corresponds to Mn_2O_3 and Mn_3O_4.

$$3Mn_2O_3 + H_2 \rightarrow 2Mn_3O_4 + H_2O \tag{4}$$

$$Mn_3O_4 + H_2 \rightarrow 3MnO + H_2O \tag{5}$$

In contrast to pure CeO_2 and MnO_x, the reduction profiles of Ce_xMn_{1-x} catalysts are more complicated. For Ce_xMn_{1-x}, the TPR profiles consist of three overlapping peaks at lower temperature and one peak at higher temperature. According to the reduction characteristics of pure MnO_x and CeO_2, it can be deduced that the lower temperature peaks (182/351 °C, 189/340 °C, 169/343 °C) are assigned to the two-step reduction of Mn_2O_3. The peaks at 693 °C or 714 °C are attributed to the oxygen species in bulk CeO_2. It is worthy to note that another obvious peak at lower temperature (295 °C, 283 °C or 232 °C) as shown in Figure 5b is possible to be caused by the synergistic effect between Mn^{2+}/Mn^{3+} and Ce^{4+}, which is related with CeO_2-MnO_x solid solution. It can facilitate the mobility of the oxygen species in the Ce_xMn_{1-x} composite oxide. Therefore, their catalytic activities over benzene are higher than pure CeO_2 and MnO_x. Additionally, the reduction temperature is lower and the peak corresponding to the oxygen species in bulk CeO_2 disappear in the TPR pattern of $Ce_{0.3}Mn_{0.7}$ compared with those of $Ce_{0.7}Mn_{0.3}/Ce_{0.5}Mn_{0.5}$. This indicates that the reduction of the manganese oxide and the cerium oxide in $Ce_{0.3}Mn_{0.7}$ is promoted more obvious, which results in the highest activity over benzene in the Ce_xMn_{1-x} composite oxides. In the view of hydrogen consumption, the same conclusion can be also obtained. $Ce_{0.3}Mn_{0.7}$ consumed the most hydrogen gas (4.88447 mmol/g) among Ce_xMn_{1-x} composite oxides indicating that $Ce_{0.3}Mn_{0.7}$ possesses more oxygen species, which are beneficial to benzene oxidation reaction. Therefore, $Ce_{0.3}Mn_{0.7}$ presents higher activity compared with other Ce_xMn_{1-x}.
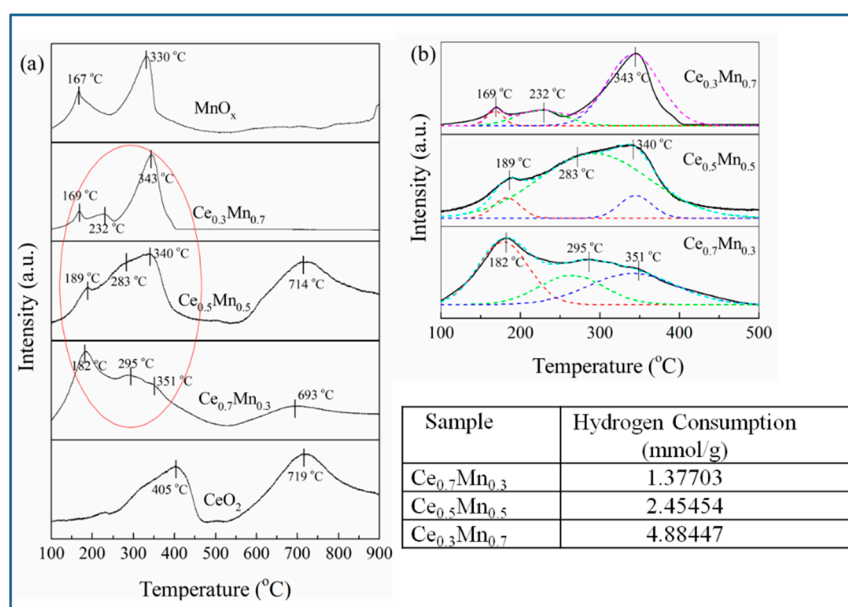

Figure 5. H_2-TPR of CeO_2, MnO_x, Ce_xMn_{1-x} (**a**) and Enlarged picture of the red circle area (**b**).

3.3. Factors Influencing the Catalytic Activity

Through the analysis, it has been acquired that $Ce_{0.3}Mn_{0.7}$ performs excellently in catalytic oxidation of benzene among the Ce_xMn_{1-x} catalysts. Many factors are considered to determine catalytic performances. Firstly, the existence of Ce-Mn solid solution results in the formation of oxygen vacancies due to incorporate Mn into CeO_2 crystal lattice, which can enhance their activities. Secondly, the large numbers of active sites will be introduced after removal of oxalate chains, because

of the formation of porous structure which can also facilitate the adsorption and diffusion of organic molecules, thus reducing limitations of interphase mass transfer and promoting their catalytic activities. Thirdly, the better reducibility at low temperature also plays a great role in the catalytic activity. Through the analysis of TPR, it has been acquired that the reductions of Ce_xMn_{1-x} catalysts start at the lower temperature compared with CeO_2, which indicate that the catalysts possess more highly reducible surface species such as absorbed oxygen. Additionally, the existence of special peak caused by the strong interaction between Ce and Mn compared with MnO_x also result in the enhancement of reducibility. Finally, the oxidation of organic molecules over transition metal oxide or mixed metal oxide catalysts involves two identical mechanisms: a Langmuir–Hinshelwood mechanism at lower temperature and a Mars–van Krevelen mechanism with increasing reaction temperature [28,40]. At lower temperature, the adsorbed oxygen species with higher activity can enhance the adsorption and oxidation of VOCs. With the temperature rising, the adsorbed organic molecules are oxidized by the oxygen of metal oxides, which can be replenished by gas phase oxygen. Therefore, the adsorbed oxygen species will have an important role to play in determining its catalytic activity. As displayed in Table 2, the $Ce_{0.3}Mn_{0.7}$ exhibits a higher content of Ce^{4+} and Mn^{3+}. The high-valence of cerium and manganese ions are preferred to adsorb more active oxygen species to attend in the reaction, thereby $Ce_{0.3}Mn_{0.7}$ possessed higher activity.

4. Conclusions

A series of Ce_xMn_{1-x} composite oxides, CeO_2 and MnO_x were synthesized through oxalate method and the complete catalytic oxidation of benzene were examined. The results indicated that Ce_xMn_{1-x} catalysts exhibited better activities comparing with pure CeO_2 or MnO_x, among which the catalytic activity reached the best when the Ce_{at}/Mn_{at} optimum ratio was 3:7. In order to identify the advantage of oxalate route, Ce-Mn composite oxides were also synthesized through carbonate method and hydrothermal method. The results indicated that the samples prepared by oxalate route exhibited higher activities, which were probably related with the microstructure of catalyst. Additionally, the influence of oxygen vacancy and synergistic effect in the benzene catalytic oxidation can't be also ignored.

References

1.　Garcia, T.; Solsona, B.; Cazorla-Amoros, D.; Linares-Solano, A.; Taylor, S.H. Total oxidation of volatile organic compounds by vanadium promoted palladium-titania catalysts: Comparison of aromatic and polyaromatic compounds. *Appl. Catal. B Environ.* **2006**, *62*, 66–76. [CrossRef]

2.　Tang, X.F.; Xu, Y.D.; Shen, W.J. Promoting effect of copper on the catalytic activity of MnO_x-CeO_2 mixed oxide for complete oxidation of benzene. *Chem. Eng. J.* **2008**, *144*, 175–180. [CrossRef]

3.　Einaga, H.; Futamura, S. Comparative study on the catalytic activities of alumina-supported metal oxides for oxidation of benzene and cyclohexane with ozone. *React. Kinet. Catal. Lett.* **2004**, *81*, 121–128. [CrossRef]

4.　Einaga, H.; Ogata, A. Benzene oxidation with ozone over supported manganese oxide catalysts: Effect of catalyst support and reaction conditions. *J. Hazard. Mater.* **2009**, *164*, 1236–1241. [CrossRef] [PubMed]

5. Einaga, H.; Teraoka, Y.; Ogat, A. Benzene oxidation with ozone over manganese oxide supported on zeolite catalysts. *Catal. Today* **2011**, *164*, 571–574. [CrossRef]

6. Liotta, L.F.; Ousmane, M.; Di Carlo, G.; Pantaleo, G.; Deganello, G.; Boreave, A.; Giroir-Fendler, A. Catalytic Removal of Toluene over Co_3O_4-CeO_2 Mixed Oxide Catalysts: Comparison with Pt/Al_2O_3. *Catal. Lett.* **2009**, *127*, 270–276. [CrossRef]

7. Liotta, L.F.; Ousmane, M.; Di Carlo, G.; Pantaleo, G.; Deganello, G.; Marci, G.; Retailleau, L.; Giroir-Fendler, A. Total oxidation of propene at low temperature over Co_3O_4-CeO_2 mixed oxides: Role of surface oxygen vacancies and bulk oxygen mobility in the catalytic activity. *Appl. Catal. A Gen.* **2008**, *347*, 81–88. [CrossRef]

8. Lojewska, J.; Kolodziej, A.; Lojewski, T.; Kapica, R.; Tyczkowski, J. Structured cobalt oxide catalyst for VOC combustion. Part I: Catalytic and engineering correlations. *Appl. Catal. A Gen.* **2009**, *366*, 206–211. [CrossRef]

9. Walerczyk, W.; Zawadzki, M. Structural and catalytic properties of $Pt/ZnAl_2O_4$ as catalyst for VOC total oxidation. *Catal. Today* **2011**, *176*, 159–162. [CrossRef]

10. Zwinkels, M.F.M.; Jaras, S.G.; Menon, P.G.; Griffin, T.A. Catalytic Materials for High-Temperature Combustion. *Catal. Rev.-Sci. Eng.* **1993**, *35*, 319–358. [CrossRef]

11. Lahousse, C.; Bernier, A.; Grange, P.; Delmon, B.; Papaefthimiou, P.; Ioannides, T.; Verykios, X. Evaluation of gamma-MnO_2 as a VOC removal catalyst: Comparison with a noble metal catalyst. *J. Catal.* **1998**, *178*, 214–225. [CrossRef]

12. Dai, Q.G.; Wang, X.Y.; Lu, G.Z. Low-temperature catalytic combustion of trichloroethylene over cerium oxide and catalyst deactivation. *Appl. Catal. B Environ.* **2008**, *81*, 192–202. [CrossRef]

13. Kim, H.J.; Choi, S.W.; Inyang, H.I. Catalytic oxidation of toluene in contaminant emission control systems using Mn-Ce/γ-Al_2O_3. *Environ. Technol.* **2008**, *29*, 559–569. [CrossRef]

14. Saqer, S.M.; Kondarides, D.I.; Verykios, X.E. Catalytic Activity of Supported Platinum and Metal Oxide Catalysts for Toluene Oxidation. *Top. Catal.* **2009**, *52*, 517–527. [CrossRef]

15. Qi, G.S.; Yang, R.T. Performance and kinetics study for low-temperature SCR of NO with NH_3 over MnO_x-CeO_2 catalyst. *J. Catal.* **2003**, *217*, 434–441. [CrossRef]

16. Qi, G.S.; Yang, R.T.; Chang, R. MnO_x-CeO_2 mixed oxides prepared by co-precipitation for selective catalytic reduction of NO with NH_3 at low temperatures. *Appl. Catal. B Environ.* **2004**, *51*, 93–106. [CrossRef]

17. Silva, A.M.T.; Marques, R.R.N.; Quinta-Ferreira, R.M. Catalysts based in cerium oxide for wet oxidation of acrylic acid in the prevention of environmental risks. *Appl. Catal. B Environ.* **2004**, *47*, 269–279. [CrossRef]

18. Tang, X.F.; Li, Y.G.; Huang, X.M.; Xu, Y.D.; Zhu, H.Q.; Wang, J.G.; Shen, W.J. MnO_x-CeO_2 mixed oxide catalysts for complete oxidation of formaldehyde: Effect of preparation method and calcination temperature. *Appl. Catal. B Environ.* **2006**, *62*, 265–273. [CrossRef]

19. Wang, Z.; Shen, G.L.; Li, J.Q.; Liu, H.D.; Wang, Q.; Chen, Y.F. Catalytic removal of benzene over CeO_2-MnO_x composite oxides prepared by hydrothermal method. *Appl. Catal. B Environ.* **2013**, *138*, 253–259. [CrossRef]

20. Wang, Z.; Yang, M.; Shen, G.L.; Liu, H.D.; Chen, Y.F.; Wang, Q. Catalytic removal of benzene over CeO_2-MnO_x composite oxides with rod-like morphology supporting PdO. *J. Nanopart. Res.* **2014**, *16*, 2367. [CrossRef]

21. Tang, W.X.; Wu, X.F.; Li, S.D.; Li, W.H.; Chen, Y.F. Porous Mn-Co mixed oxide nanorod as a novel catalyst with enhanced catalytic activity for removal of VOCs. *Catal. Commun.* **2014**, *56*, 134–138. [CrossRef]

22. Zhang, R.Z.; Dai, H.X.; Du, Y.C.; Zhang, L.; Deng, J.G.; Xia, Y.S.; Zhao, Z.X.; Meng, X.; Liu, Y.X. P123-PMMA Dual-Templating Generation and Unique Physicochemical Properties of Three-Dimensionally Ordered Macroporous Iron Oxides with Nanovoids in the Crystalline Walls. *Inorg. Chem.* **2011**, *50*, 2534–2544. [CrossRef]

23. Chen, X.; Shen, Y.F.; Suib, S.L.; O'Young, C.L. Characterization of manganese oxide octahedral molecular sieve (M-OMS-2) materials with different metal cation dopants. *Chem. Mater.* **2002**, *14*, 940–948. [CrossRef]

24. Pfau, A.; Schierbaum, K.D. The Electronic-Structure of Stoichiometric and Reduced CeO_2 Surfaces—An XPS, UPS and HREELS Study. *Surf. Sci.* **1994**, *321*, 71–80. [CrossRef]

25. Xiao, W.D.; Guo, Q.L.; Wang, E.G. Transformation of CeO_2 (111) to Ce_2O_3 (0001) films. *Chem. Phys. Lett.* **2003**, *368*, 527–531. [CrossRef]

26. Lenormand, F.; Hilaire, L.; Kili, K.; Krill, G.; Maire, G. Oxidation-State of Cerium in Cerium-Based Catalysts Investigated by Spectroscopic Probes. *J. Phys. Chem.* **1988**, *92*, 2561–2568. [CrossRef]

27. Machida, M.; Uto, M.; Kurogi, D.; Kijima, T. MnO_x-CeO_2 binary oxides for catalytic NO_x sorption at low temperatures. Sorptive removal of NO_x. *Chem. Mater.* **2000**, *12*, 3158–3164. [CrossRef]

28.   Santos, V.P.; Pereira, M.F.R.; Orfao, J.J.M.; Figueiredo, J.L. The role of lattice oxygen on the activity of manganese oxides towards the oxidation of volatile organic compounds. *Appl. Catal. B Environ.* **2010**, *99*, 353–363. [CrossRef]

29.   Rao, T.; Shen, M.Q.; Jia, L.W.; Hao, J.J.; Wang, J. Oxidation of ethanol over Mn-Ce-O and Mn-Ce-Zr-O complex compounds synthesized by sol-gel method. *Catal. Commun.* **2007**, *8*, 1743–1747. [CrossRef]

30.   Dula, R.; Janik, R.; Machej, T.; Stoch, J.; Grabowski, R.; Serwicka, E.M. Mn-containing catalytic materials for the total combustion of toluene: The role of Mn localisation in the structure of LDH precursor. *Catal. Today* **2007**, *119*, 327–331. [CrossRef]

31.   Han, Y.F.; Chen, F.X.; Zhong, Z.Y.; Ramesh, K.; Chen, L.W.; Widjaja, E. Controlled synthesis, characterization, and catalytic properties of Mn_2O_3 and Mn_3O_4 nanoparticles supported on mesoporous silica SBA-15. *J. Phys. Chem. B* **2006**, *110*, 24450–24456. [CrossRef]

32.   Luo, Y.; Deng, Y.Q.; Mao, W.; Yang, X.J.; Zhu, K.K.; Xu, J.; Han, Y.F. Probing the Surface Structure of α-Mn_2O_3 Nanocrystals during CO Oxidation by Operando Raman Spectroscopy. *J. Phys. Chem. C* **2012**, *116*, 20975–20981. [CrossRef]

33.   Galakhov, V.R.; Demeter, M.; Bartkowski, S.; Neumann, M.; Ovechkina, N.A.; Kurmaev, E.Z.; Logachevskaya, N.I.; Mukovskii, Y.M.; Mitchell, J.; Ederer, D.L. Mn 3s exchange splitting in mixed-valence manganites. *Phys. Rev. B* **2002**, *65*, 113102. [CrossRef]

34.   Wang, H.; Zhu, H.Q.; Qin, Z.F.; Liang, F.X.; Wang, G.F.; Wang, J.G. Deactivation of a Au/CeO_2-Co_3O_4 catalyst during CO preferential oxidation in H_2-rich stream. *J. Catal.* **2009**, *264*, 154–162. [CrossRef]

35.   Wu, Y.S.; Zhang, Y.X.; Liu, M.; Ma, Z.C.C. Complete catalytic oxidation of o-xylene over Mn-Ce oxides prepared using a redox-precipitation method. *Catal. Today* **2010**, *153*, 170–175. [CrossRef]

36.   Trovarelli, A. Catalytic properties of ceria and CeO_2-containing materials. *Catal. Rev.* **1996**, *38*, 439–520. [CrossRef]

37.   Aneggi, E.; Boaro, M.; de Leitenburg, C.; Dolcetti, G.; Trovarelli, A. Insights into the redox properties of ceria-based oxides and their implications in catalysis. *J. Alloy Compd.* **2006**, *408*, 1096–1102. [CrossRef]

38.   Tana; Zhang, M.L.; Li, J.; Li, H.J.; Li, Y.; Shen, W.J. Morphology-dependent redox and catalytic properties of CeO_2 nanostructures: Nanowires, nanorods and nanoparticles. *Catal. Today* **2009**, *148*, 179–183. [CrossRef]

39.   Tang, X.F.; Chen, J.L.; Li, Y.G.; Li, Y.; Xu, Y.D.; Shen, W.J. Complete oxidation of formaldehyde over Ag/MnO_x-CeO_2 catalysts. *Chem. Eng. J.* **2006**, *118*, 119–125. [CrossRef]

40.   Tang, W.X.; Wu, X.F.; Li, D.Y.; Wang, Z.; Liu, G.; Liu, H.D.; Chen, Y.F. Oxalate route for promoting activity of manganese oxide catalysts in total VOCs' oxidation: Effect of calcination temperature and preparation method. *J. Mater. Chem. A* **2014**, *2*, 2544–2554. [CrossRef]